Experimental Investigation of the Effect of Rake on a Bluff Body Equipped with a Diffuser

Pawel Kekus-Kumor[1,2] and David Angland[2]

[1] *Department of Aerodynamics, Lukasiewicz Research Network — Institute of Aviation, al. Krakowska 110/114, Warsaw, 02-256, Poland*
[2] *Faculty of Engineering and Physical Sciences, University of Southampton, Burgess Road, Southampton, SO16 7QF, United Kingdom*

Abstract

This article presents the results of an experimental investigation into the impact of rake, or inclination of the underfloor, on the aerodynamics of a bluff body equipped with an underbody diffuser. An extensive wind tunnel campaign, utilising a remotely-actuated model for faster data acquisition, showed that introducing rake results in a downforce increase at all ride heights and diffuser angles, with the strongest effect occurring at low ride heights. Surface pressure measurements on the underbody revealed this to be caused by three main effects. First, a large increase in loading at the front of the floor, due to the inclination of the floor with rake angle and subsequently an increase in the pressure pumping effect. Second, a reduction in the suction peak at the throat of the diffuser, which leads to reduced pressure recovery in the diffuser, and less likely separation at high diffuser angles or low ride heights. Third, stronger streamwise vortices along the edges of the underfloor and diffuser, which generate downforce directly due to their low-pressure cores, but also introduce upwash under the model, further inhibiting separation in the diffuser. As the related drag penalty is minimal, aerodynamic efficiency is also improved with increasing rake angle.

Keywords: diffuser, wind tunnel, ground effect, vortices, automotive

1 Introduction

Diffusers, in an automotive context are passive devices located at the rear of a car's underfloor, commonly used in racing cars for generating downforce, and hence improving on-track performance [1, 2]. A simple schematic of an underbody diffuser is presented in Fig. 1. Since diffusers first appeared, a number of academic studies looked into the mechanisms of downforce generation using a flat underfloor equipped with a diffuser, and into how the performance is influenced by various parameters, including ride height, i.e. the separation between the ground and the body, and diffuser angle. It was established through wind tunnel testing that a diffuser-equipped, flat-roofed Ahmed body [3] in ground effect generates downforce through three inter-related mechanisms, two of which are illustrated in Fig. 1 [4]:

- Surface upsweep, which effectively cambers the body, resulting in a downward force.
- Ground interaction, where the flow underneath the body is accelerated due to the ground constraint and its static pressure decreases. The magnitude of the pressure reduction increases with decreasing ground separation, up until a critical ride height, where viscous forces become dominant and the effect is reversed.
- Diffuser pressure pumping, where the increasing cross-sectional area results in decreasing flow velocity and increasing static pressure. In the case of a bluff body or a car with a fixed base pressure at the diffuser exit, the pressure recovery manifests itself as a suction peak at the diffuser inlet, which propagates upstream, towards the front of the body [4–9]. This phenomenon is illustrated in Fig. 2.

A key milestone in the understanding of ground effect diffuser flows was the discovery, aided by flow visualisation, of counter-rotating vortices near the side edges of the diffuser [11]. It was shown that these vortices, shown in Fig. 3, not only help to prevent or delay flow separation at the sharp diffuser inlet edge [7, 9, 11–14], but also directly contribute to downforce generation by inducing low-pressure regions on the sides of the diffuser surface [6, 9, 10, 12]. The vortices were also shown to grow in size while moving inboard and towards the diffuser ramp as they propagate downstream through the diffuser channel, and in some cases to detach from the diffuser surface [8, 14–16].

1.1 The Impact of Ride Height and Diffuser Angle

Further experiments and CFD simulations confirmed that the effect of reducing the ride height of a diffuser-equipped bluff body in ground effect is an increase in downforce at a growing rate [4, 6–10, 15, 17–19]. This is mainly the result of increased pressure recovery, which results in a stronger suction peak at the diffuser inlet, and stronger vortices [6–10, 12, 18]. However, Cooper et al. and Jowsey and Passmore [4, 18] also observed a sharp change in the streamwise pressure recovery rate in the vicinity of the leading edge of the underfloor. At high ground separations, the pressure recovery rate changed suddenly due to a separation bubble. As ride height was reduced, the favourable pressure gradient under the nose increased, diminishing the localised separation. This resulted in more gradual pressure recovery in that area, and therefore reduced pressure under the front half of the underfloor and increased net downforce.

As ride height is reduced further, the increasing adverse pressure gradient in the diffuser causes the flow to separate. However, the counter-rotating vortices prevent separation near the sides of the diffuser, and help to reattach the separated flow in the centre of the diffuser further downstream, resulting in a localised separation bubble. Simultaneously, an onset of vortex breakdown occurs, characterised by increased vortex size, and substantially reduced axial and cross-flow velocities and vorticity [10]. These changes cause a reduction of the downforce enhancement rate, or a small decrease in downforce, jointly referred to as the downforce plateau [6–10, 15, 18].

At even lower ride heights, downforce continues to increase despite the presence of the separation bubble, which gradually moves towards the diffuser inlet. At the critical ride height, the separation bubble is swept to one side, causing asymmetric vortex breakdown and flow separation at the inlet over a substantial part of the diffuser width, resulting in a large recirculation region and a significant loss of downforce [6–10, 12, 15]. Ehirim et al. [8, 9, 16] also observed that the direction of the asymmetric stall depends on the relative strength of the vortices prior to breakdown, with the stronger vortex surviving the subsequent stall. Furthermore, Ruhrmann and Zhang, Zhang et al. and Ehirim [7, 10, 20] observed that the process of downforce loss is subject to significant hysteresis at diffuser angles of 15° and above, as the vortices re-form and reattach the flow at higher ride heights than when they break down.

Curves of downforce coefficient with respect to non-dimensional ride height, obtained experimentally by Howell, Cooper et al., and Ruhrmann and Zhang [4, 7, 21] and computationally by Knight et al. [19], also show that, as the diffuser angle is increased, the initial downforce reduction occurs at progressively higher ride heights. Importantly, ride height and diffuser angle jointly determine the diffuser area ratio, which is defined as the ratio of cross-sectional areas of the outlet and the inlet of the diffuser. This non-dimensional parameter directly controls the pressure recovery, and hence the adverse pressure gradient in the diffuser. Therefore, as the diffuser angle is increased, so is the area ratio and the resulting adverse pressure gradient, causing flow separation at a higher ride height [7, 15]. At diffuser angles below 10°, the adverse pressure gradient is small enough that the separation bubble does not form, and downforce keeps increasing until the asymmetric stall.

1.2 The Impact of Rake

Rake, defined as the angle between the underfloor and the ground, is commonly used in race cars, yet the published body of knowledge regarding the impact of rake on diffuser performance is limited. The majority of existing studies on rake examined its effect by pitching the entire model, rather than just the underfloor. Although this method is analogous to raking an entire race car by modifying suspension geometry, it potentially obscures the changes in aerodynamic performance of the bottom of the model by also inclining the top surface. In the current study, the effect of inclining the whole body is removed as only the underfloor is inclined, allowing this effect of be isolated.

George [11] found that the relationship between downforce and rake angle is approximately linear for angles between ±30°, for a body in the freestream with a 20° diffuser and no end plates. Furthermore, significant changes in the flow behaviour were reported, including the formation of counter-rotating vortices along the entire length of the body at rake angles of 10° and above. However, the high rake angles used in that study are not applicable to racing cars, and no results were presented at rake angles lower than 5°.

Cooper et al. [4] varied the ride height of the model at rake angles of 1.60° and 2.75°, and found that the increase in downforce coefficient due to a 1.60° rake grew from 0.1 at a high ground separation to 0.4 near the critical ride height, suggesting that ground effect significantly amplifies the effect of rake. However, the effect of increasing rake to 2.75° was much weaker. Furthermore, the downforce loss phenomenon at low ride heights was eliminated at both rake angles, suggesting that the benefits of rake are two-fold—not only does it generate additional downforce, but it also broadens the diffuser's performance envelope. However, the causes behind this trend were not discussed.

The only previous investigation into the impact of inclining the underfloor while keeping the roof parallel to the ground was presented by Kekus and Angland [22], in a work that investigated hardware-in-the-loop optimisation. The authors of that study used a model with actuated ride height, rake angle and diffuser angle to generate performance maps with respect to those three degrees of freedom. However, the study was carried out with a static ground, an atypical model geometry, and a relatively low Reynolds number (0.66×10^6), making comparisons with other studies difficult.

A shortcoming of existing studies on rake is the lack of data on performance trends and flow pattern variations when the underfloor is raked in isolation, with the rest of the model parallel to the ground, in order to separate the effects of inclining the different surfaces. In this paper, we present the results from a comprehensive wind tunnel campaign, with more than 3500 test points, where we investigated the effect of varying the ride height, rake and diffuser angles of a flat-roofed Ahmed body suspended above a moving ground. Static pressure on the underside of the body was measured at every data point, with the aim of interpreting the force data and quantifying the role of the vortices in the downforce generation. The paper begins with a description of the experimental methodology. The baseline, zero rake results are presented next, and the trends in downforce, aerodynamic efficiency and centre of pressure are discussed for various diffuser angles, in order to establish regimes of diffuser angles where the behaviour is similar. Then, the effect of rake is discussed relative to the zero-rake baseline for three different diffuser angle regimes.

2 Methodology

2.1 Wind Tunnel Facility

The experiments were performed in a closed-circuit, low-speed wind tunnel at the University of Southampton, the same facility where a number of previous diffuser studies took place [6, 7, 10, 11, 15]. The test section has a 2.15 m by 1.57 m cross-section with chamfered corners and a length of 4.4 m, and is equipped with a moving ground. The moving ground was run at a speed equal to the freestream velocity during all tests, to ensure correct boundary conditions under the model. This had been shown to be essential, as an additional boundary layer on the ground surface has a significant impact on quantitative diffuser performance [4–7, 11, 12, 20, 21]. The freestream and moving ground velocities were controlled with a precision of ±0.05 m/s, and the freestream turbulence level was 0.2% [6]. A more detailed description of the wind tunnel and the moving ground assembly was presented by Burgin et al. [23].

2.2 Model Design and Setup

In order to facilitate rapid data acquisition, linear actuators were incorporated into the design of the model, permitting on-the-fly adjustments not only of the ride height, but also of the rake and diffuser angles, without the need to stop the wind tunnel to manually adjust or replace components.

This solution allowed data collection for up to 1400 configurations per day, resulting in greatly increased resolution compared to a conventional system. In order to maintain shape accuracy under aerodynamic loading, the model and its supporting structure were designed for stiffness, with high-strength materials and precise mechanical actuators.

The model, shown mounted in the wind tunnel in fig. 4, was a cuboid with a width of $W = 400\,\mathrm{mm}$, a height of $H = 310\,\mathrm{mm}$, a length of $L_M = 800\,\mathrm{mm}$, and a 64 mm radius on all four sides of the nose, as shown in fig. 5. These dimensions have similar ratios to the models used by Cooper et al., Breslouer and George, and Desai et al. [4, 13, 17], and are identical to the model of Jowsey and Passmore [18]. The frontal areas of the model ($S = 0.124\,\mathrm{m}^2$) and the supporting structure and struts ($\sim 0.043\,\mathrm{m}^2$) resulted in a total blockage ratio of $\sim 5.1\%$. In order to avoid end plates along the entire length of the underfloor at a positive rake angle, the diffuser end plates themselves had to incline together with the underfloor. To achieve this, a double-sidewall system was used. The main pair of sidewalls, tapered towards the rear of the model, was mounted directly to the roof and nose of the model. The angle of the taper was such that the plane of the underfloor would be below the bottom edge of the sidewalls even at the maximum rake angle. An additional pair of sidewalls was mounted directly to the underfloor, and filled the gap between the underfloor and the main sidewalls, as well as constituted end plates for the diffuser. The two sets of sidewalls, machined out of transparent acrylic, are clearly visible in fig. 5b.

The model was suspended from a supporting frame by four Actuonix L16-P-63 linear actuators, which were used to control the ride height, h_1, defined as the height of the lowest point of the model above the ground. The attainable range of ride heights was between 10 mm and 90 mm above the moving ground, or between $h_1/H = 0.032$ and 0.290 in non-dimensional form; lower ride heights were not used to avoid the model touching the moving ground as it was actuated. h_2 and h_3 in fig. 5a denote the heights above the ground of the diffuser inlet and outlet respectively. The supporting frame was mounted to a force transducer, which was attached to wind tunnel struts. An additional steel plate was mounted between the force transducer and the struts, which was used to anchor the structure to wind tunnel walls, reducing vibrations of the model and allowing precise adjustments of its yaw angle.

The bottom of the model was comprised of two carbon fibre plates. The 536 mm-long underfloor was hinged to the nose, and its angle relative to the ground was modified by an Actuonix L16-P-150 linear actuator, mounted between the underfloor and the roof of the model. The 200 mm-long diffuser plate was hinged to the underfloor, their relative angle controlled by an identical actuator, mounted between the two plates. The underfloor was hinged directly to the nose. The maximum rake angle of $\gamma = 5°$ was chosen to cover the range typically used in race cars, and the maximum diffuser angle of $\theta = 40°$ was constrained by the model's roof. Although diffusers were previously examined at angles only up to 30°, the addition of rake was expected to broaden the performance envelope of the diffuser, so data was collected for the entire 40° range.

The model had an open tail cavity, i.e. there was no surface connecting the trailing edge of the diffuser plate and the trailing edge of the roof, as seen in fig. 5. This configuration was required to modify the rake and diffuser angles automatically in real-time, and therefore to enable such a large parameter sweep, but is inconsistent with the models used by past investigators, which utilised variable-length diffuser plates that extended to the same streamwise position as the roof, and were joined to the roof with vertical plates. A quantitative comparison between configurations with an open and closed tail cavity was carried out by Kekus [24], and the results showed minor variations of the surface pressure coefficient at the diffuser outlet, but with negligible impact on the performance and flow features observed under the model. Therefore, the results of this study may be compared directly to those using closed-tail models, and the trends of the baseline case without rake are comparable with existing studies.

The model was installed with the roof parallel to the ground and the sidewalls parallel to the wind tunnel walls, with uncertainties on pitch, roll and yaw angles of $\pm 0.2°$, $\pm 0.3°$ and $\pm 0.2°$ respectively. The uncertainties of ride height, rake and diffuser angles were $\pm 0.7\,\mathrm{mm}$, $\pm 0.1°$ and $\pm 0.9°$ respectively, which includes their deflections due to aerodynamic loading.

2.3 Force and Surface Pressure Measurements

Forces and moments exerted on the model were measured using an ATI Delta 6-component transducer. The directions of positive drag force, side force and downforce are along the x, y and z axes respectively, whereas the directions of the rolling, pitching and yawing moments are around those respective axes according to the right-hand rule, and their origin is at the centre of the frontal plane of the nose, which is also the origin of the coordinate system. The axes and the location of the origin are specified in figure 5a.

The underfloor and diffuser plates were pressure-tapped along the centreline of the model in the streamwise direction. In addition, there were two spanwise series of taps, 100 mm upstream and downstream of the diffuser inlet. Metallic tubes embedded in the plates were connected to two 64-channel Scanivalve ZOC33 differential pressure scanners with a ±2500 Pa sensing range and an accuracy of 0.15% of the full-scale. The reference pressure channels were connected to the static pressure channel of a pitot-static tube in the freestream. Both pressure scanners were calibrated at two temperatures, across the entire sensing range, to within ±5 Pa, which is assumed to be the uncertainty of the pressure measurements.

2.4 Testing Procedure and Data Processing

All tests were carried out at a freestream velocity of 20 m/s, which corresponds to a length-based Reynolds number of $Re = 1.1 \times 10^6$, and was restricted by the mechanical limitations of the actuators and the sensing range of the pressure scanners. Previous studies using similar geometries were performed at $Re = 0.83 \times 10^6$ [4] and 2.2×10^6 [18], and most other diffuser studies used values between $Re = 1.8 \times 10^6$ and 2.7×10^6 [6–9, 15, 16]. In order to reduce potential sensitivity to Reynolds number, transition on the underside of the body was fixed with a 0.35 mm-diameter wire, fixed to the underfloor 16 mm downstream of the leading edge of the underfloor ($x/L_M = 0.1$).

Sweeps of ride height were performed for several values of rake and diffuser angles, which were known to be configurations of interest thanks to initial low-fidelity sampling and previously published results. Likewise, sweeps of rake and diffuser angles were performed for several values of the remaining degrees of freedom. Each sweep was carried out in both directions, i.e. gradually decreasing and increasing ride height, or gradually increasing and decreasing the rake and diffuser angles, in order to establish the extent of hysteresis in the system. Full force and pressure measurements were taken at every data point.

A datum configuration was tested at the beginning and at the end of each sweep, to track long-term repeatability of the force and moment measurements. The datum was defined as the maximum ride height ($h_1 = 90$ mm) and zero rake and diffuser angles, as this configuration is not susceptible to hysteresis with respect to any of the three degrees of freedom.

Wind-off tare measurements with the model installed were taken at a set of ride heights and rake and diffuser angles, in order to take into account the shifting centre of mass of the model. The data was then interpolated and subtracted from each wind-on measurement. Next, this procedure was repeated with the model removed, to establish the aerodynamic loads generated by the supporting frame, for the entire range of ride height actuator extensions. Both total and frame-only aerodynamic loads were then divided by freestream dynamic pressure q_∞, taken from a pitot-static tube at the time of each measurement, obtaining $C_F S$ and $C_M S L_M$ forms, where C_F and C_M are force and moment coefficients respectively. The frame-only loads were then subtracted from the total loads, and finally divided by $S = 0.124\,\text{m}^2$ and $SL_M = 0.0992\,\text{m}^3$, to obtain aerodynamic force and moment coefficients of the model respectively. The direction of the coefficient of downforce, denoted as C_L, is towards the ground, following an established convention [7, 10, 15, 17, 25].

Pressure readings were calibrated using the temperature taken at the time of each measurement, interpolating between the obtained calibration curves, and subsequently non-dimensionalised by q_∞. Ride height h_1 was non-dimensionalised by model height H, following the convention applied to similar geometries by Cooper et al. and Jowsey and Passmore [4, 18, 26]. However, h_1/d, where d is model half-width, is indicated on a secondary axis where possible, to enable a more convenient comparison with other studies [6–10, 15, 20].

3 Results and Discussion

A single sweep of ride height consisted of reducing the ride height from the maximum of $h_1/H = 0.290$ down to 0.032 (indicated by solid lines), and increasing it back up to 0.290 (indicated by dashed lines). For the rake and diffuser sweeps, the respective angles were increased from 0° to their maximums (solid lines), and then reduced back to 0° (dashed lines).

Although the ride height sweeps at zero rake are similar to those presented in previous publications [4,18], they are discussed below in order to form a baseline for the discussion of the impact of rake on the flow features and performance of a diffuser. Also, the on-surface pressure measurements allow some phenomena to be explained in more detail. The changes relative to this baseline introduced with rake are discussed in the next section.

3.1 Behaviour at Zero Rake

3.1.1 Downforce

Figure 6 shows the measurements of downforce at zero rake as a function of ride height. The general trend is an increase in downforce with increasing diffuser angle and decreasing ride height, as expected. The behaviour of the downforce of different diffuser angles with ride height can be grouped into three distinct regimes. The first regime corresponds to diffuser angles of $\theta = 6.2°$ and 11.2°, which both show similar behaviour. As the ride height decreases, the downforce and the rate of downforce increase ($\mathrm{d}C_L/\mathrm{d}h_1$) both increase. The gradient $\mathrm{d}C_L/\mathrm{d}h_1$ reaches a maximum at a particular ride height. Below this ride height, the downforce continues to increase as the gradient decreases, until it reaches a maximum where $\mathrm{d}C_L/\mathrm{d}h_1 = 0$. Subsequently, at lower ride heights there is a downforce reduction. The higher diffuser angle produces more downforce at all ride heights up to the ride height corresponding to maximum downforce. This trend and behaviour has been reported for both wings and diffusers in ground effect.

The behaviour in the second regime is shown at the diffuser angle of $\theta = 16.3°$. The behaviour shows a distinctive reduction and then a plateau in the downforce centred around a ride height of $h_1/H = 0.17$. This results in this diffuser angle producing less downforce than the lower diffuser angle of 11.2° below a particular ride height, as shown in fig. 6. There is then a small increase in downforce up to the maximum downforce $C_{L_{\max}}$, resulting in a characteristic downforce plateau across this ride height range. This behaviour was not observed at lower diffuser angles.

The third distinctive type of behaviour is exhibited by the diffuser angle of $\theta = 24.7°$. This diffuser angle produces significantly less downforce than the lower diffuser angles across the entire ride height map.

At zero rake, there is no significant hysteresis with decreasing and increasing ride height. The only exception is the second regime (the diffuser angle of $\theta = 16.3°$, which exhibited the plateau), where some hysteresis is present at the ride height corresponding to $C_{L_{\max}}$. For decreasing ride height, the maximum downforce occurs at a slightly lower ride height than for the case where the ride height was increasing.

The behaviour in these three different regimes can be explained by examining the pressure distributions at two different ride heights (figs. 7 and 8). The first ride height (shown in fig. 7) is at a relatively large value of $h_1/H = 0.236$. The streamwise pressure distributions are characterised by two low pressure peaks (fig. 7a). There is a strong suction peak at the underfloor leading edge, caused by the relatively sharp curvature of the nose. The second low pressure peak is at the inlet of the diffuser. The suction peak at the diffuser inlet is a result of the discontinuity in the curvature of the diffuser and the subsequent streamwise expansion and the corresponding pressure increase to the exit pressure behind the model.

As ride height is reduced at a fixed diffuser angle, the diffuser area ratio h_3/h_2 is increased, leading to more severe pressure recovery, a stronger suction peak at the inlet (seen at $\theta = 6.2°$ and 11.2° in fig. 8a), and increased downforce. It can be seen that the exit pressure at the base of the bluff body is approximately constant for all the diffuser angles except for the highest one, where the diffuser is completely stalled and produces little downforce. Through the action of pressure pumping, this pressure recovery in the diffuser results in additional suction under the majority of the underfloor ($x/L_M < 0.75$), as seen in fig. 8a. This is typical behaviour for a bluff body equipped with a diffuser and has been reported previously (see Section 1). At the highest diffuser angle ($\theta = 24.7°$), there is no peak at the inlet of the diffuser or subsequent pressure recovery, demonstrating the flow is separated at the throat of the diffuser.

The spanwise pressure distributions in figs. 7 and 8 can be used to determine the strength and influence of the edge vortices. At the relatively large ride height, $h_1/H = 0.236$ (figs. 7b and 7c), the behaviour is consistent except at the diffuser angle of $\theta = 24.7°$, where the flow is separated in the diffuser as discussed above. Upstream of the diffuser inlet ($x/L_M = 0.625$), there is little evidence of strong suction due to edge vortices. However, flow entrainment around the edges of the underfloor causes locally increased C_p, manifested in the spanwise pressure gradients at $x/L_M = 0.625$, hitherto referred to as suction leakage. At the diffuser angles of $\theta = 11.2°$ and 16.3°, traces of vortex-induced suction may be observed at the edges of the underfloor, suggesting weak vortices have already started at this ride height. In the diffuser ($x/L_M = 0.875$), there is clear evidence of counter-rotating vortices that increase in strength and size with increasing diffuser angle, further increasing the total downforce. The role of the vortices in producing downforce and in keeping the flow attached has been discussed in Section 1.

Corresponding pressure distributions at a low ride height of $h_1/H = 0.046$ are shown in fig. 8. At this ride height, the diffusers where the flow was attached are all producing less than their maximum downforce, although at values that are close to that maximum. The loading on the floor upstream of the diffuser inlet ($x/L_M < 0.75$) is greater than at the higher ride height, as is the suction peak at the diffuser inlet, except at $\theta = 16.3°$. The net result of this is an increase in downforce relative to the higher ride height of $h_1/H = 0.236$. It will be seen later, in plots of centre of pressure, that this change in loading corresponds to a slight shift forward in the centre of pressure.

Flow entrainment around the edges of the underfloor again causes suction leakage at $x/L_M = 0.625$. There is evidence of strong vortices for the low diffuser angles of 6.2°, as shown in fig. 8c. At the diffuser angle of 11.2°, asymmetric vortex breakdown occurs. This phenomenon has been previously reported by others, e.g. Zhang et al. [10]. At the higher diffuser angles of 16.3° and 24.7° there is complete vortex breakdown at the streamwise location of $x/L_M = 0.875$, with no low pressure associated with vortex cores, resulting in a further loss of downforce, as discussed previously. The 24.7° diffuser was fully separated at all ride heights, with no pressure recovery in the diffuser and flat spanwise pressure profiles.

The last trend to explain in the baseline downforce data is the plateau at the diffuser angle of 16.3°, which is not seen at the other diffuser angles. A streamwise pressure distribution plot at two ride heights is shown in fig. 9. The first ride height corresponds to the maximum of the plateau at $h_1/H = 0.236$ seen previously. This is compared to the lower ride height of $h_1/H = 0.168$, where downforce has decreased, before it subsequently increases again at even lower ride heights. At the higher ride height, the diffuser produces a large suction peak. As ride height decreases, the pressure distribution shows that there is a significant area of separation in the diffuser at 16.3° due to the increased adverse pressure gradient. This changes the pressure recovery in the diffuser and reduces the suction peak at the throat, reducing the diffuser's performance. This also causes a weakening of the edge vortices (data omitted for brevity, but a similar effect can be seen at an even lower ride height in fig. 8). However, this reduction in the diffuser is offset by an increase in the loading over the front of the underfloor at the lower ride height. The balance between these two competing trends leads to the characteristic plateau in the downforce behaviour at this ride height.

3.1.2 Aerodynamic Efficiency

The trends in aerodynamic efficiency (the ratio of downforce to drag, L/D) are shown in fig. 10b. Drag increases at a much slower rate than downforce with decreasing ride height (fig. 10a). Therefore, the shape of the efficiency curves is strongly correlated to the downforce curves discussed previously. The general trend is an increase in efficiency as ride height is reduced, until it reaches a peak. At lower ride heights, the efficiency decreases as downforce slows down and then decreases, while drag continues to increase. The highest L/D ratio occurs at the diffuser angle of 11.2°. The maximum efficiency value is approximately 2.5 at the non-dimensional ride height h_1/H of 0.1. At this diffuser angle, this maximum of aerodynamic efficiency occurs at a higher ride height than the maximum downforce ($h_1/H = 0.07$). This is due to the rate of drag increase ($\mathrm{d}C_D/\mathrm{d}h_1$)

continuing to increase at lower ride heights, as shown in fig. 10a. As mentioned previously, the diffuser angle of 16.3° was characterised by a plateau in downforce. For this diffuser angle, the maximum efficiency occurred at a higher ride height, before this plateau occurred.

3.1.3 Centre of Pressure

The centre of pressure is relatively constant as the ride height decreases, as shown in fig. 11. An exception to this was the high diffuser case at an angle of $\theta = 24.7°$. At this diffuser angle the flow was separated, and the large suction peak at the inlet of the diffuser was not present. This lack of suction towards the rear of the body resulted in a shift of the centre of pressure forward of approximately $x/L_M = 30\%$ compared to the other diffuser angles. At the diffuser angle of $\theta = 6.2°$ there was also a slight forward movement of the centre of pressure (8% difference over the ride height range measured) as ride height was reduced. This was due to the strengthening of the suction peaks at the leading edge of the underfloor and at the inlet of the diffuser, as seen in the streamwise pressure distributions in figs. 7 and 8. The reason for the downforce plateau at the diffuser angle of 16.3° was explained by a loss of downforce at the rear of the floor. The centre of pressure data also shows this effect. At a ride height of h_1/H of 0.24, before the plateau occurs, the centre of pressure is slightly rearward compared to the lower ride heights, where the centre of pressure shifts slightly upstream.

3.1.4 Summary

The downforce behaviour for the zero rake case can be divided into three distinct regimes. At low diffuser angles there is a an increase in downforce and the rate of downforce increase with decreasing ride height, up to a maximum. As ride height is reduced further, the downforce gradient decreases, until a downforce reduction occurs. At a moderate diffuser angle ($\theta = 16.3°$) there was a plateau region where the downforce peaked and reduced slightly, before increasing again. This was caused by a loss of downforce in the diffuser as ride height decreased. This reduction was compensated by an increase in the loading on the underfloor. Finally, at a high diffuser angle ($\theta = 24.7°$), there was a total loss of downforce due to separation off the diffuser throat.

The underfloor only showed very weak vortices at certain diffuser angles and experienced significant suction leakage towards the edges of the bluff body. Strong vortices were observed in the diffuser. Vortex breakdown occurred at low ride heights, and for the diffuser angle of $\theta = 11.2°$ this breakdown was asymmetric in the diffuser. Next, the effect of rake on these behaviours will be investigated and quantified.

3.2 Effect of Rake

3.2.1 Low Diffuser Angles

In this section the diffuser angles of 6.2° and 11.4° are discussed, based on data from sweeps of rake angle. As outlined in the previous section, the behaviour with decreasing ride height was representative of the typical behaviour of wings and diffusers in ground effect, with an increase in downforce and the rate of downforce, up to a maximum rate of downforce. As ride height was reduced further, the rate of downforce decreased, until the maximum downforce occurred. Subsequently, there was a force reduction. The rake sweep data is presented as trends in downforce, L/D and centre of pressure as a function of rake angle. The ride height of $h_1/H = 0.129$ and the diffuser angle of 6.2° were chosen for visualisation, as the behaviour of both diffuser angles was similar, as discussed in Section 3.1.

Figure 12 shows the effect of rake angle at the ride height of $h_1/H = 0.129$. This behaviour is similar to one seen across the whole ride height range, i.e. $0.0645 < h_1/H < 0.1935$. The general trend is an increase in downforce from $C_L = 0.360$ at zero rake to $C_L = 0.573$ at a rake angle of 4.8°. There is no hysteresis with rake angle for this diffuser angle. The gradient of the change in downforce with rake angle reduces as the rake angle increases. The L/D ratio also increases significantly with rake angle, from 1.39 at zero rake to 2.12 at the rake angle of 4.8°. The ratio of this increase is almost identical to the increase in downforce over this rake angle range. Therefore, drag remains relatively unchanged with changes in rake angle — only a 5.3% increase takes place when increasing rake from zero to the maximum. Therefore, the L/D ratio is driven almost entirely by the increase in downforce. The centre of pressure has the trend of moving upstream as the rake angle increases. There is a forward shift in the balance of approximately 20% upstream from zero rake to the rake angle of 4.8°.

The aerodynamic reasons for these changes can be found by examining the pressure distributions at two different rake angles, at the same diffuser angle and ride height, as shown in fig. 13.

Introducing rake into the geometry has three main effects on the pressure distributions. The first is a large increase in the loading at the front of the floor due to the inclination of the floor. This enhances the pressure pumping effect, reducing the pressure on the upstream section of the underfloor. This has a significant effect on the overall load generated, and is also responsible for the upstream shift in centre of pressure with increasing rake angle. The second effect is the reduced pressure recovery in the diffuser, resulting in a significantly weaker suction peak at the diffuser inlet. This reduced pressure recovery demand makes the diffuser less likely to stall at lower ride heights. This tendency becomes clearer at the higher diffuser angles, discussed later, where the diffuser was fully stalled for the zero rake case. The third effect can be observed upstream of the diffuser inlet (fig. 13b), where strong streamwise vortices exist at $\gamma = 4.8°$, whereas no evidence of such vortices was present for the zero rake case. These vortices grow stronger with increasing rake angle. They increase loading towards the edges of the underfloor due to their low pressure cores (vortex-induced suction). They also introduce an upwash, reducing the local angle of attack and helping the flow to remain attached. This is similar to the mechanism proposed by Zhang et al. [10] at zero rake. However, this mechanism is enhanced with the introduction of rake due to the stronger vortices.

3.2.2 Moderate Diffuser Angles

In this section the results at the diffuser angle of 16.3° are discussed. At this diffuser angle, the downforce versus ride height behaviour with zero rake was characterised by a plateau region. Again, the trends with an increase in rake angle were common across the different ride heights and there was no hysteresis with varying rake angle. The effect of changing rake angle is similar to the low diffuser angle, and is shown in fig. 14. The increase in downforce over the rake angle range is greater than at low diffuser angles (78% increase in downforce compare to 59% for the low diffuser angle of 6.2°), which means that the effect of rake becomes more prominent as the diffuser angle is increased. The pressure distribution data presented in fig. 15 shows that this is due to stronger edge vortices generated along the floor and in the diffuser, amplifying the effect discussed for low diffuser angles.

The increase in drag was greater with the higher diffuser angle (10% compared to only 5.3% at the low diffuser angle). However, similar to the low diffuser angle, the increase in downforce dominated, and there was an increase in the L/D ratio of 61% over the rake angle range. This is greater than the 51% increase for the low diffuser angle, because in spite of the larger increase in drag with rake angle for this diffuser angle, the increase in downforce is greater. Similar to the low diffuser angle, the increases in downforce and aerodynamic efficiency are not a linear function of the rake angle, with low rake angles giving a greater increase relative to high rake angles. This can most clearly be seen in the L/D behaviour. While the zero rake results showed the downforce versus ride height behaviour was fundamentally different between the low and medium diffuser cases, the effect of rake on the zero rake behaviour was very similar.

The centre of pressure shifted forward by 25%, from $x_{CP}/L_M = 0.53$ to 0.39, over the range of rake angles tested. This is greater than the low diffuser angle case and is caused by the increase in loading at the front of the underfloor, as is shown in the pressure distributions in fig. 15.

At this diffuser angle, the three main effects of rake previously seen at low diffuser angles are again present, i.e. the increased loading at the front of the floor, the smaller pressure recovery in the diffuser, and the appearance of edge vortices along the edges of the raked underfloor. The suction peak at the inlet of the diffuser is more pronounced than at the lower diffuser angle, but it is still smaller than in the zero rake case, resulting in a smaller pressure recovery demand in the diffuser and a reduced likelihood of stall at low ride heights. A fourth effect can be seen at this medium diffuser angle, which explains why rake becomes more effective at higher diffuser angles. Both at the underfloor and in the diffuser itself, the vortices that existed at the lower diffuser angle are now much stronger. This has two effects. One is to increase the loading towards the spanwise edges of the body, and the second is to reduce the likelihood of separation in the diffuser at low ride heights due to the upwash the vortices induce. Increasing the rake angle makes these vortices and their effect even stronger.

3.2.3 High Diffuser Angles

In this section the diffuser angle of 24.7° is discussed. The behaviour with rake is different to what was observed earlier for the low and medium diffuser angles, and is presented in fig. 16. At this diffuser angle there is some hysteresis with respect to rake angle between $\gamma = 0.7°$ and 2.6°. Above and below these rake angles, the hysteresis disappears. Similar to the other diffuser angles, the behaviour with rake does not fundamentally change with ride height and so only one ride height is presented. A low ride height of $h_1/H = 0.065$ was chosen, since the largest effects of rake angle are observed at this ride height. At this diffuser angle the diffuser was completely stalled at zero rake, and the downforce produced was negligible, as discussed previously in Section 3.1.1. Since the baseline at zero rake generates so little downforce, there is a large increase with increasing rake angle (600% over the rake angle range investigated). There is a very large initial increase up to a rake angle of 1.3°, where the diffuser becomes unstalled. As the rake angle is increased further, downforce continues to increase, but at a much lower gradient with respect to the rake angle. Similar to the other diffuser angles, drag increases, but a much smaller rate than downforce, and therefore the L/D ratio also increases with an increase in rake angle. The hysteresis is associated with the critical rake angle where the diffuser becomes unstalled. This occurs between rake angles of 0.7° and 1.3°.

The centre of pressure when the diffuser is completely stalled at zero rake is far forward, at $x_{CP}/L_M = 0.2$, as previously discussed in Section 3.1.3. Once the diffuser starts producing a pressure recovery, the centre of pressure moves rearward by 20%, up to $x_{CP}/L_M = 0.4$. Higher rake angles produce a similar effect as for the other diffuser angles discussed, where increasing the rake angle produces more loading at the front of the underfloor, and the centre of pressures moves forward by up to 17%.

The mechanism by which rake causes the diffuser to produce a pressure recovery, even though it is completely stalled at zero rake, can be seen by inspecting the pressure distributions in fig. 17.

At zero rake, the diffuser is completely stalled and there is no pressure recovery. This results in the low downforce levels at this ride height, as seen in Section 3.1.1. As the rake angle is increased, more loading is produced at the front of the underfloor, as previously identified for the other diffuser angles. Increasing the rake angle above a critical angle also causes the diffuser to become unstalled, as was also seen in the force data in fig. 16. At a rake angle of 4.8°, strong pressure recovery is present in the diffuser. A rake angle of 1.3° was not sufficient to obtain a proper pressure recovery in the diffuser, and the exit pressure was lower due to the lack of this pressure recovery. This weakens the mechanism of pressure pumping under the floor, resulting in less downforce. Once the rake angle is high enough to cause a pressure recovery in the diffuser, there is a large increase in downforce, as seen in the force data.

The area of hysteresis identified in the force measurements was due to this transition between the diffuser being stalled and being able to generate a pressure recovery. The vortices generated on the underfloor when introducing rake, and the upwash they produce, are responsible for keeping the flow attached at a diffuser angle where the flow was fully stalled at zero rake. These vortices under the floor were too weak to be identified in the measurements at zero rake, but they become stronger with an increase in rake angle. At the rake angle of 1.3° they are of insufficient strength and the diffuser is still stalled. There is a significant asymmetry in the vortices under the floor (fig. 17b), which gets more pronounced as the rake angle is increased. Similar behaviour has previously been identified for diffusers at zero rake close to stall [8, 9]. At the rake angle of 4.8° there is evidence of vortex burst and a significant flow asymmetry in the diffuser. The vortex at $y/W = -0.4$ has completely disappeared (fig. 17c), and the spanwise pressure profile between $y/W = 0.1$ and -0.5 is identical to the fully stalled case at zero rake. At the other side of the diffuser ($y/W = 0.40$) a strong vortex still exists, producing significant loading. Again, similar behaviour has previously been identified for diffusers close to stall at zero rake. While the zero rake case was stalled, the introduction of rake was able to reattach the flow due to the upwash produced by the vortices under the rake floor.

4 Conclusion

The impact of rake, or an inclination of the underfloor, on the performance and flow features of a diffuser-equipped bluff body in ground effect was investigated using a wind tunnel model with variable ride height, rake and diffuser angles. Downforce was measured with respect to changing ride height and rake angle at several diffuser angles, which represent different flow regimes. Furthermore, streamwise and cross-flow profiles of surface pressure on the underbody were measured at every data point to allow the flow features responsible for the changes to be identified.

The baseline data at zero rake showed similar trends to those previously reported for similar geometries. In the current work, a wider range of diffuser angles was investigated, and it was shown that the diffuser was completely stalled at the highest tested diffuser angle. The baseline data was divided into three different regimes, with similar downforce behaviour with respect to ride height in each regime. The plateau regime at moderate diffuser angles was investigated in more detail using the on-surface pressure distributions to explain why this force plateau occurs. At this diffuser angle, as the ride height is reduced, there is a significant area of separation in the diffuser due to the increased adverse pressure gradient. This changes the pressure recovery in the diffuser and reduces the suction peak at the throat of the diffuser, reducing the overall aerodynamic load generated by the diffuser. This reduction in load from the diffuser is offset by an increase in the loading over the front of the underfloor at the lower ride height due to the ground effect, which increases at lower ride heights. The balance between these two competing trends, at the front and rear of the model, is what results in the characteristic plateau in downforce for this diffuser angle regime. It also explains why the centre of pressure shifts upstream at the ride heights where the downforce plateau occurs.

Introducing rake increases the overall level of downforce produced. There are three main mechanisms responsible for this. Firstly, there is a significant increase in loading experienced by the front of the underfloor, which is also responsible for a forward shift in the centre of pressure. This was caused by the inclination of the underfloor and the subsequent pressure recovery along the entire length of the underfloor. Secondly, raking the underfloor reduces the suction peak at the throat of the diffuser. This causes a reduction in the pressure recovery demand in the diffuser for a given diffuser angle and ride height. This delays stall with respect to ride height and diffuser angle, resulting in higher peak downforce. The third effect is that the streamwise counter-rotating vortices that form along the edges of the floor and diffuser are strengthened significantly with the introduction of rake. In addition to generating downforce directly due to their low-pressure cores, these vortices introduce upwash in the diffuser and underfloor, reducing the local angle of attack and inhibiting flow separation on the diffuser and floor. This mechanism is already known for diffusers in ground effect, but it is shown here that it is enhanced significantly with the introduction of rake due to the stronger streamwise vortices.

Increasing the rake angle increased the downforce due to those three mechanisms. The downforce increase with rake angle is not a linear function. The gradient of downforce increase with rake angle decreases slightly with increasing rake angle. Therefore, proportionally more gains are achieved at lower rake angles and these gains diminish as the rake angle is increased. Increasing the rake angle also results in slightly increased drag, but at a much smaller rate than the increase in downforce. This results in a significant increase in the aerodynamic efficiency. The centre of pressure was shifted towards the front of the body when rake was increased, for all the tested ride heights and diffuser angles, due to the increased loading at the front of the underfloor. The effect of diffuser angle did not change the effect of rake angle or its mechanism. The effect of rake to delay separation and stall is most clearly seen in the configurations with low ride heights and a high diffuser angle ($\theta = 24.7°$). At zero rake, this configuration was fully stalled, but introducing sufficient rake caused a strong pressure recovery in the diffuser, and as a result, significantly more downforce in both the diffuser and underfloor. For this case, there was clearly identifiable hysteresis with rake angle. For most other diffuser angles tested, there was little or no hysteresis with rake angle for this geometry.

Nomenclature

The following symbols are used in this paper:

C_D	=	drag coefficient (-);
C_L	=	downforce coefficient (-);
$C_{L_{\max}}$	=	maximum downforce coefficient (-);
C_p	=	pressure coefficient (-);
D	=	drag force (N);
H	=	model height (m);
L	=	downforce (N);
L_M	=	model length (m);
d	=	model half-width (m);
h_1	=	ride height (m);
h_2	=	ride height at diffuser inlet (m);
h_3	=	ride height at diffuser exit (m);
x, y, z	=	coordinate system axes;
x_{CP}	=	axial centre of pressure location (m);
γ	=	rake angle (°);
θ	=	diffuser angle (°).

References

[1] J. Katz, "Aerodynamics of race cars," *Annual Review of Fluid Mechanics*, vol. 38, pp. 27–63, 2006.

[2] X. Zhang, W. Toet, and J. Zerihan, "Ground effect aerodynamics of race cars," *Applied Mechanics Reviews*, vol. 59, no. 1, pp. 33–49, 2006.

[3] S. R. Ahmed, G. Ramm, and G. Faltin, "Some salient features of the time-averaged ground vehicle wake," *SAE Technical Paper 840300*, 1984.

[4] K. R. Cooper, T. Bertenyi, G. Dutil, J. Syms, and G. Sovran, "The aerodynamic performance of automotive underbody diffusers," *SAE Technical Paper 980030*, 1998.

[5] A. Cogotti, "A parametric study on the ground effect of a simplified car model," *SAE Technical Paper 980031*, 1998.

[6] A. E. Senior and X. Zhang, "The force and pressure of a diffuser-equipped bluff body in ground effect," *Journal of Fluids Engineering*, vol. 123, no. 1, pp. 105–111, 2001.

[7] A. Ruhrmann and X. Zhang, "Influence of diffuser angle on a bluff body in ground effect," *Journal of Fluids Engineering*, vol. 125, no. 2, pp. 332–338, 2003.

[8] O. Ehirim, K. Knowles, A. Saddington, and M. Finnis, "Passive flow control on a ground-effect diffuser using an inverted wing," *SAE International Journal of Passenger Cars - Mechanical Systems*, vol. 11, no. 4, pp. 273–295, 2018.

[9] O. H. Ehirim, K. Knowles, A. J. Saddington, and M. V. Finnis, "Aerodynamics of a convex bump on a ground-effect diffuser," *ASME Journal of Fluids Engineering*, vol. 140, no. 9, 2018.

[10] X. Zhang, A. Senior, and A. Ruhrmann, "Vortices behind a bluff body with an upswept aft section in ground effect," *International Journal of Heat and Fluid Flow*, vol. 25, no. 1, pp. 1–9, 2004.

[11] A. R. George, "Aerodynamic effects of shape, camber, pitch, and ground proximity on idealized ground-vehicle bodies," *Journal of Fluids Engineering*, vol. 103, pp. 631–637, 1981.

[12] A. R. George and J. E. Donis, "Flow patterns, pressures, and forces on the underside of idealized ground effect vehicles," in *Aerodynamics of transportation - II: presented at the Joint ASME-CSME Applied Mechanics, and Fluids Engineering Conference*, vol. 7, (New York, NY, USA), pp. 69–79, ASME, 1983.

[13] S. S. Desai, C.-M. B. Lo, and A. R. George, "A computational study of idealized bluff bodies, wheels, and vortex structures in ground effect," *SAE Technical Paper 2008-01-0327*, 2008.

[14] L. S. Puglisevich and G. Page, "Large eddy simulation of the flow around a diffuser-equipped bluff body in ground effect," in *Proceedings of the ASME 2011 International Mechanical Engineering Congress & Exposition*, (Denver, CO, USA), ASME, 2011.

[15] S. Mahon, X. Zhang, and C. Gage, "The evolution of edge vortices underneath a diffuser equipped bluff body," in *12th International Symposium on Applications of Laser Techniques to Fluid Mechanics*, (Lisbon, Portugal), 2004.

[16] O. Ehirim, K. Knowles, A. Saddington, M. Finnis, and N. Lawson, "On the near-wake of a ground-effect diffuser with passive flow control," *International Journal of Automotive Technology*, vol. 20, no. 1, pp. 11–23, 2019.

[17] O. J. Breslouer and A. R. George, "Exploratory experimental studies of forces and flow structure on a bluff body with variable diffuser and wheel configurations," *SAE Technical Paper 2008-01-0326*, 2008.

[18] L. Jowsey and M. Passmore, "Experimental study of multiple-channel automotive underbody diffusers," *Proceedings of the Institution of Mechanical Engineers, Part D: Journal of Automobile Engineering*, vol. 224, no. 7, pp. 865–879, 2010.

[19] J. Knight, M. Spicak, A. Kuzenko, G. Haritos, and G. Ren, "Investigation of vehicle ride height and diffuser ramp angle on downforce and efficiency," in *Proceedings of the Institution of Mechanical Engineers, Part D: Journal of Automobile Engineering*, 2018.

[20] O. H. Ehirim, *Aerodynamics and Performance Enhancement of a Ground-effect Diffuser*. PhD thesis, Cranfield University, 2017.

[21] J. P. Howell, "The influence of ground simulation on the aerodynamics of simple car shapes with an underfloor diffuser," in *Conference on Vehicle Aerodynamics*, Royal Aerodynamic Society, 1994.

[22] P. Kekus and D. Angland, "Automatic wind tunnel-based optimisation of an automotive underbody diffuser," in *2018 AIAA Science and Technology Forum*, (Kissimmee, FL, USA), American Institute of Aeronautics and Astronautics, 2018.

[23] K. Burgin, A. P. C., and B. J. P., "Wind tunnel tests on road vehicle models using a moving belt simulation of ground effect," *Journal of Wind Engineering and Industrial Aerodynamics*, vol. 22, pp. 227–236, 1986.

[24] P. Kekus, *Aerodynamics and Experimental Optimisation of an Automotive Underbody Diffuser in the Presence of Rake*. PhD thesis, University of Southampton, 2021.

[25] A. Huminic and G. Huminic, "Aerodynamics of curved underbody diffusers using CFD," *Journal of Wind Engineering and Industrial Aerodynamics*, vol. 205: 104300, 2020.

[26] L. Jowsey, *An Experimental Study of Automotive Underbody Diffusers*. PhD thesis, Loughborough University, 2013.

List of Figures

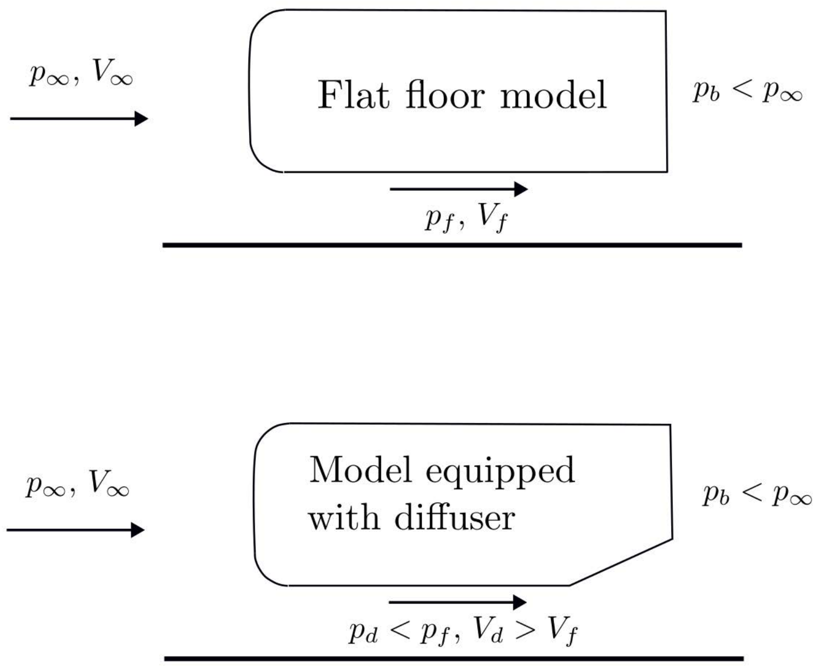

Figure 1: Schematic of the functioning of an underbody diffuser (modified from Ref. [4]). The subscript f represents conditions under a flat floor model and the subscript d represents conditions under a model equipped with a diffuser.

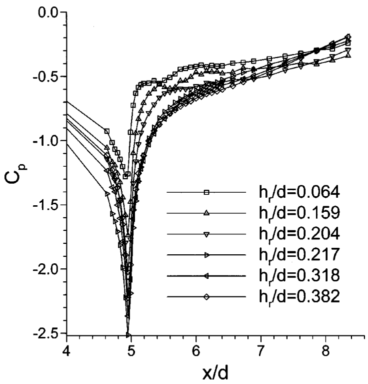

Figure 2: Surface pressure coefficient along diffuser centreline at a range of non-dimensional ride heights. Diffuser inlet at $x/d = 4.95$ [6].

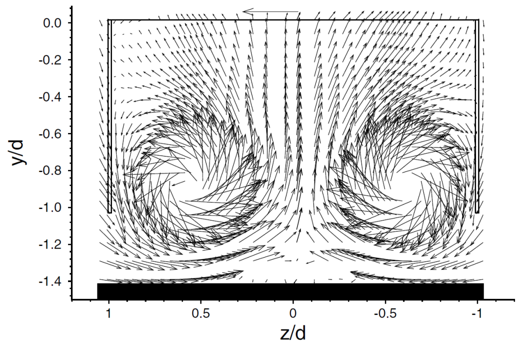

Figure 3: Mean cross-flow velocity vectors across a cross-section of the diffuser, measured using laser Doppler anemometry at $x/d = 8.476$ (15mm downstream of the model), at a non-dimensional ride height of $h_r/d = 0.382$ [10].

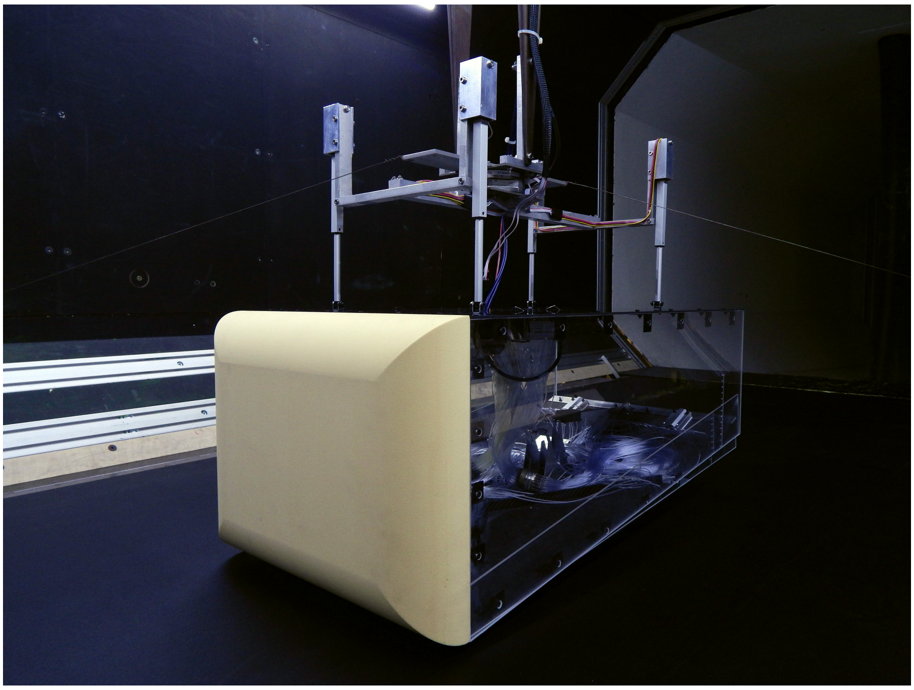

Figure 4: The diffuser model in the wind tunnel.

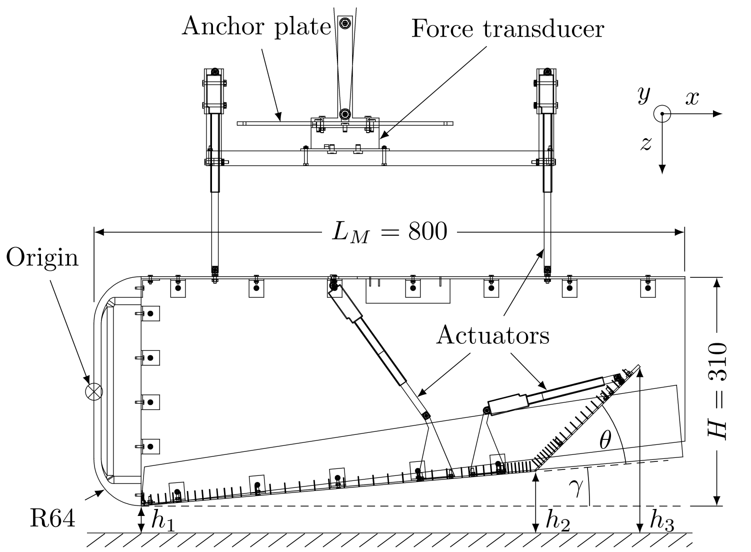

(a) Side view ($\gamma = 5°$, $\theta = 40°$), showing the definition of dimensions and the coordinate system. Streamwise locations of pressure taps are also shown. All dimensions in mm.

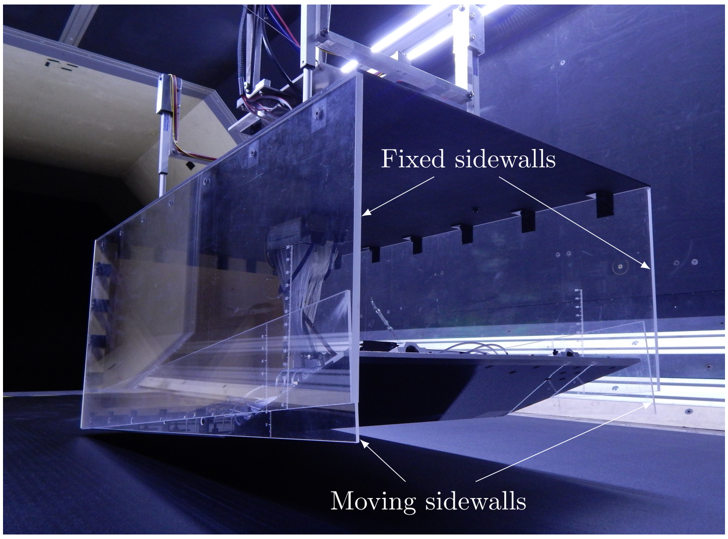

(b) Rear view in the wind tunnel, showing the double-sidewall system used to ensure the diffuser end plates were flush with the plane of the underfloor. Also visible are graduated scales engraved in the sidewalls, used for calibration of the rake and diffuser angles.

Figure 5: Details of the variable-geometry model.

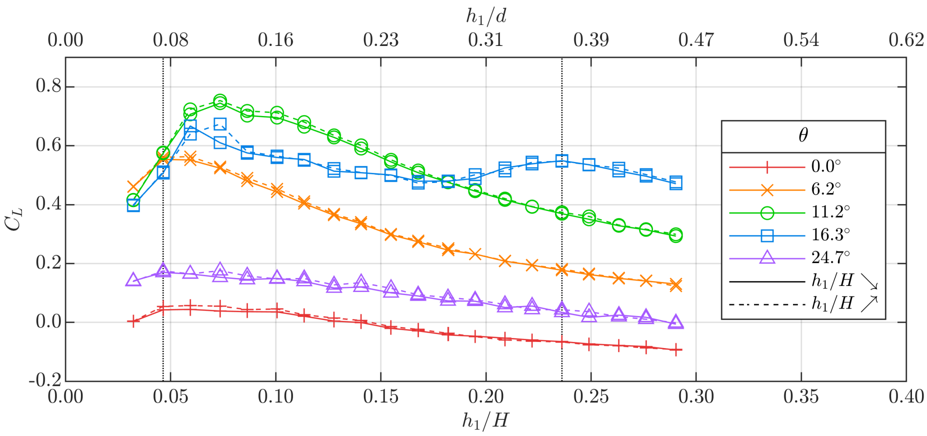

Figure 6: Plots of downforce coefficient against non-dimensional ride height, at zero rake and a range of diffuser angles. Vertical dotted lines mark ride heights displayed in figures 7 and 8.

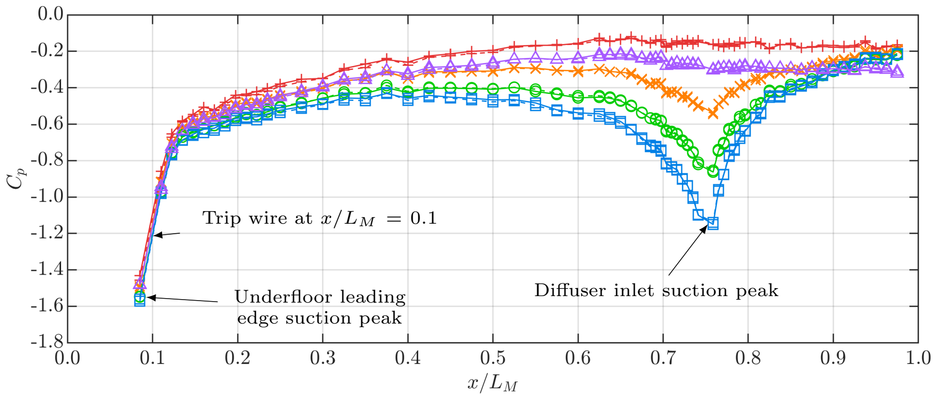

(a) Model centreline.

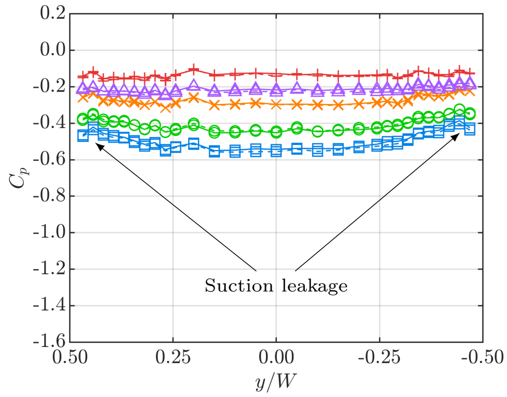

(b) Underfloor cross-section ($x/L_M = 0.625$).

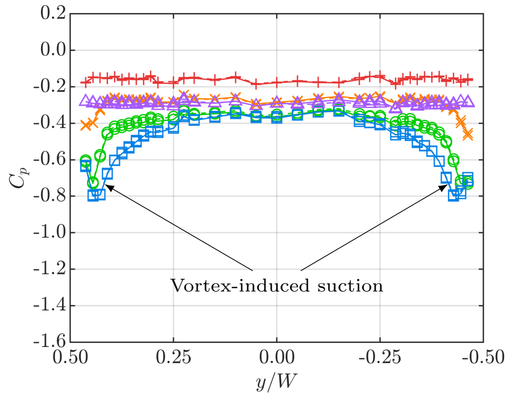

(c) Diffuser cross-section ($x/L_M = 0.875$).

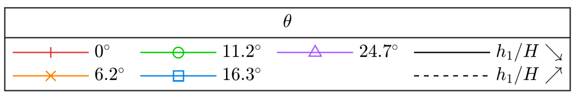

Figure 7: Plots of static pressure coefficient along the centreline and across the underfloor and the diffuser, at $h_1/H = 0.236$, $\gamma = 0°$, and a range of diffuser angles.

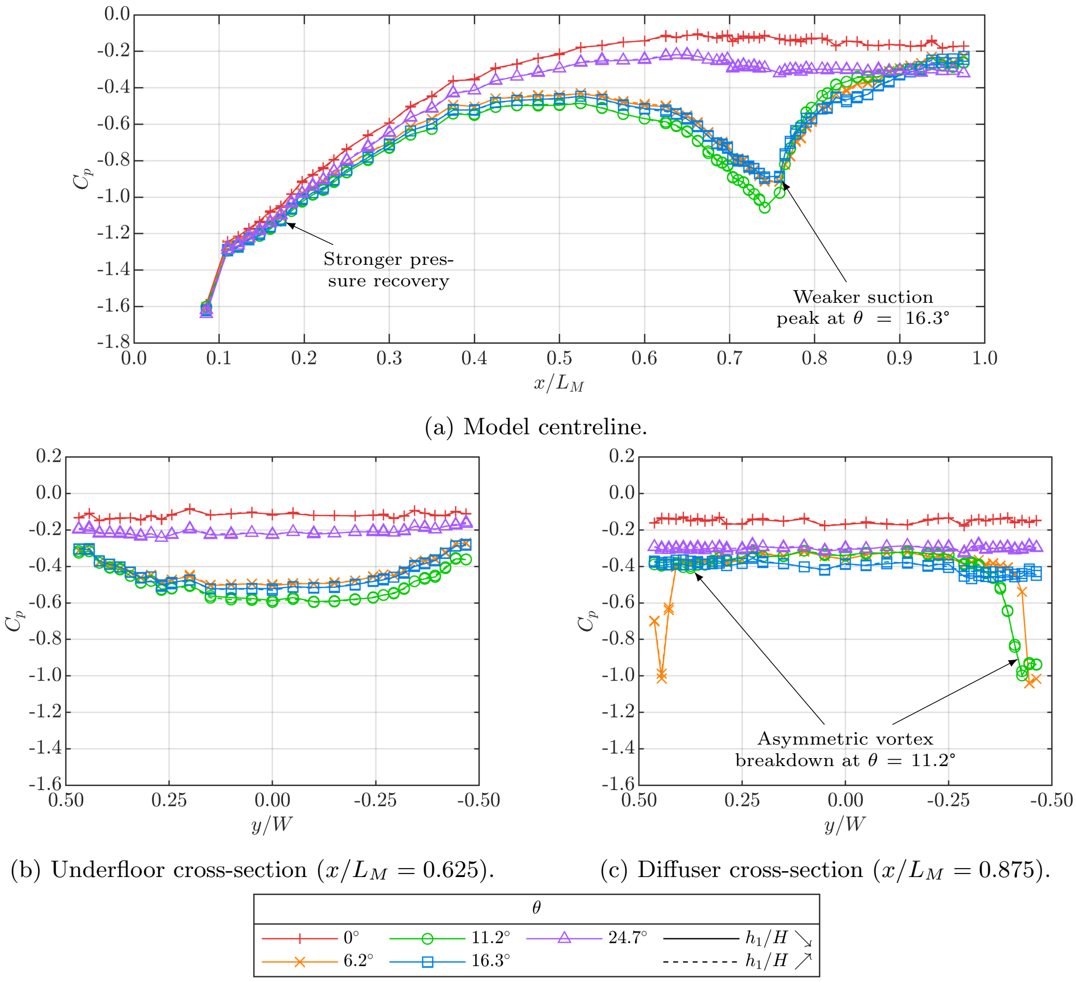

(a) Model centreline.

(b) Underfloor cross-section ($x/L_M = 0.625$).

(c) Diffuser cross-section ($x/L_M = 0.875$).

Figure 8: Plots of static pressure coefficient along the centreline and across the underfloor and the diffuser, at $h_1/H = 0.046$, $\gamma = 0°$, and a range of diffuser angles.

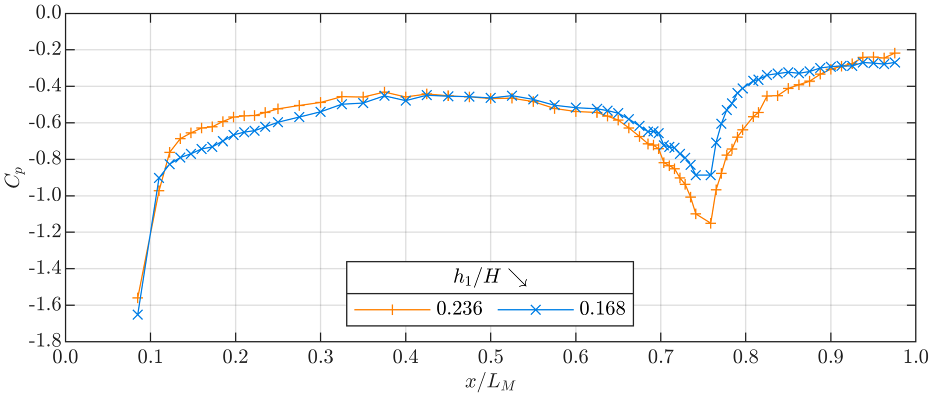

Figure 9: Streamwise static pressure distributions in the plateau regime for the diffuser angle of $\theta = 16.3°$.

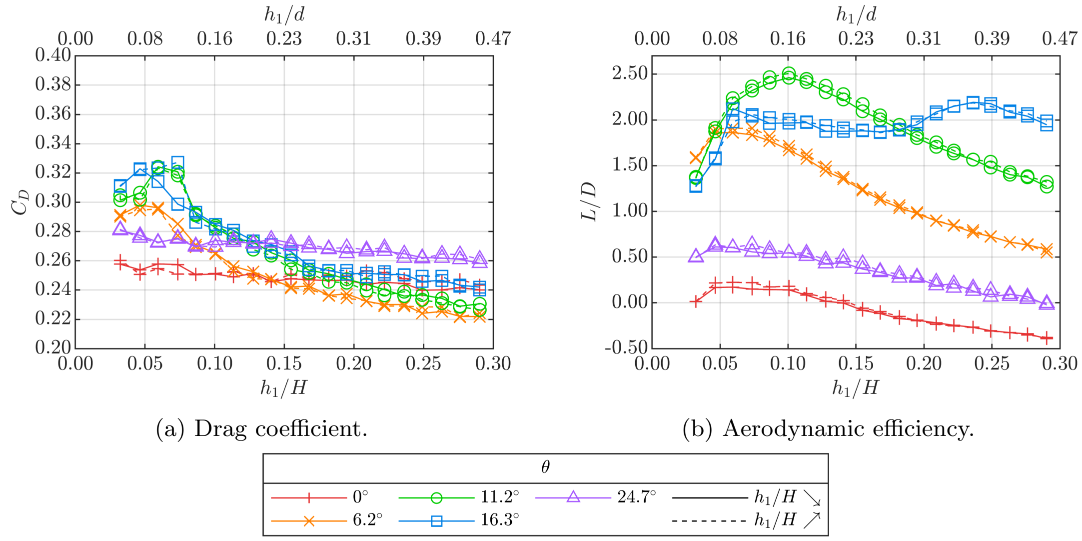

(a) Drag coefficient.

(b) Aerodynamic efficiency.

Figure 10: Plots of drag coefficient and aerodynamic efficiency against non-dimensional ride height, at zero rake and a range of diffuser angles.

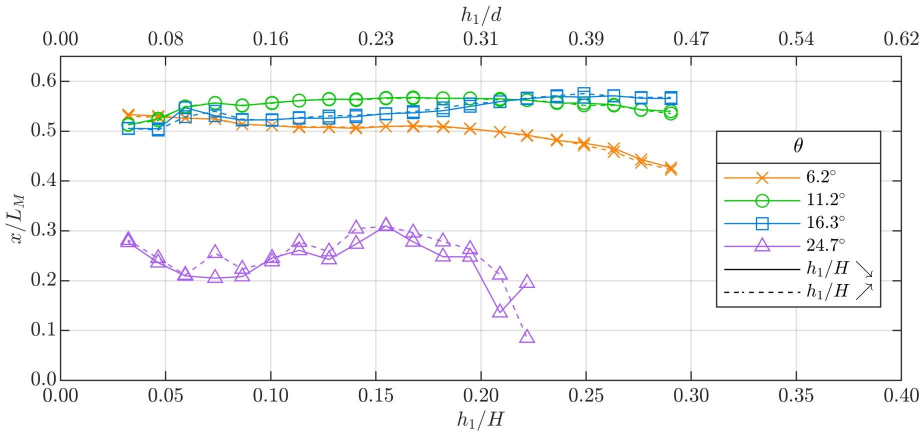

Figure 11: Plots of centre of pressure against non-dimensional ride height, at zero rake and a range of diffuser angles.

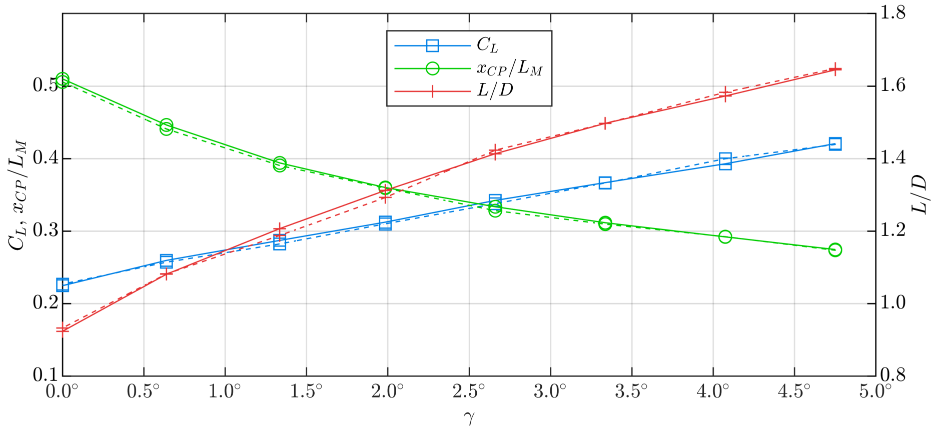

Figure 12: Plots of downforce coefficient, centre of pressure and aerodynamic efficiency against rake angle, at $h_1/H = 0.194$ and $\theta = 6.2°$.

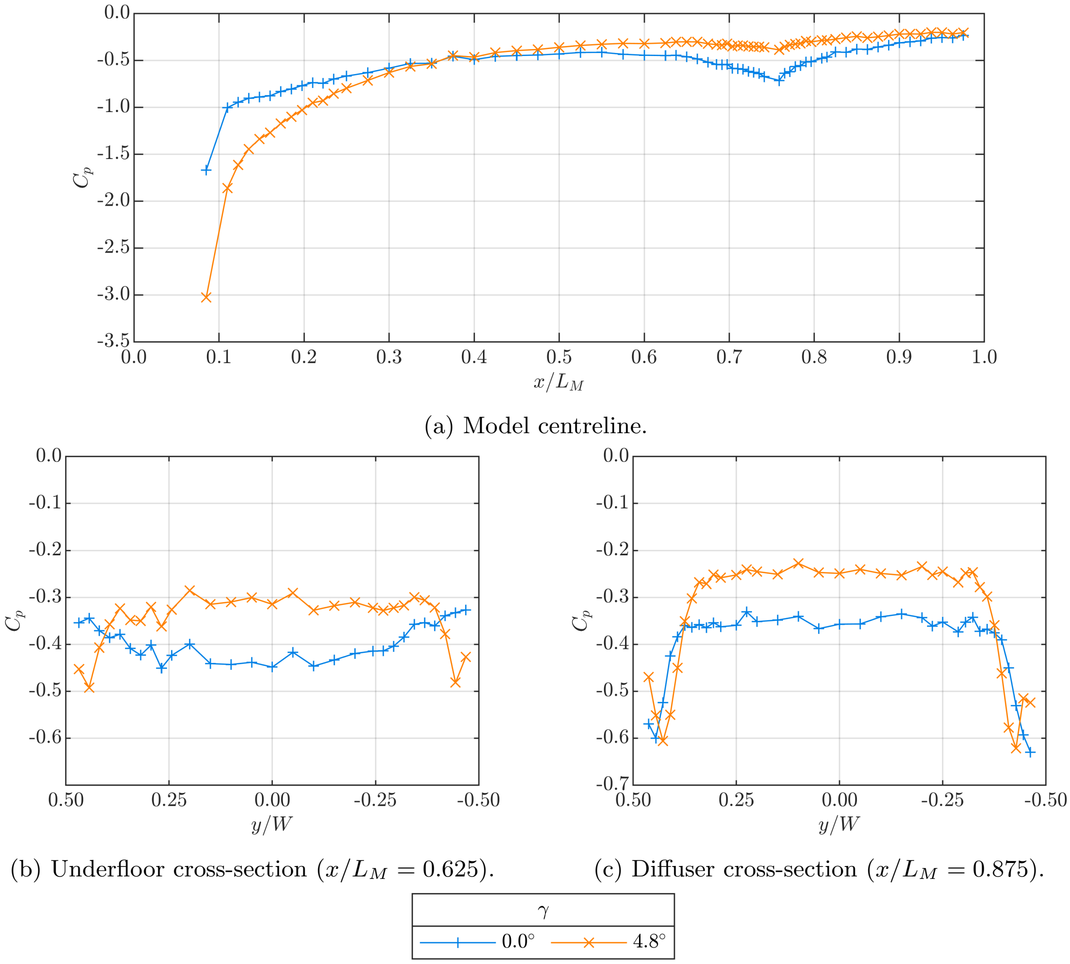

(a) Model centreline.

(b) Underfloor cross-section ($x/L_M = 0.625$).

(c) Diffuser cross-section ($x/L_M = 0.875$).

Figure 13: Plots of static pressure coefficient along the centreline and across the underfloor and the diffuser, at $h_1/H = 0.129$, $\theta = 6.2°$, and two rake angles.

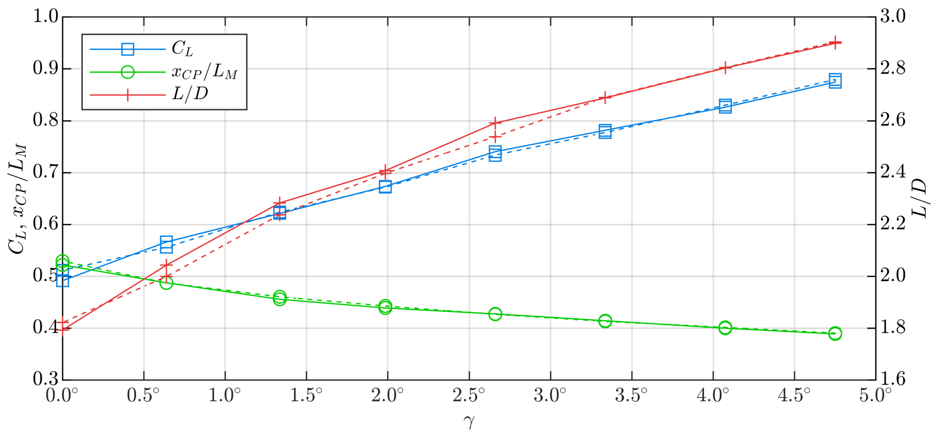

Figure 14: Plots of downforce coefficient, centre of pressure and aerodynamic efficiency against rake angle, at $h_1/H = 0.129$ and $\theta = 16.3°$.

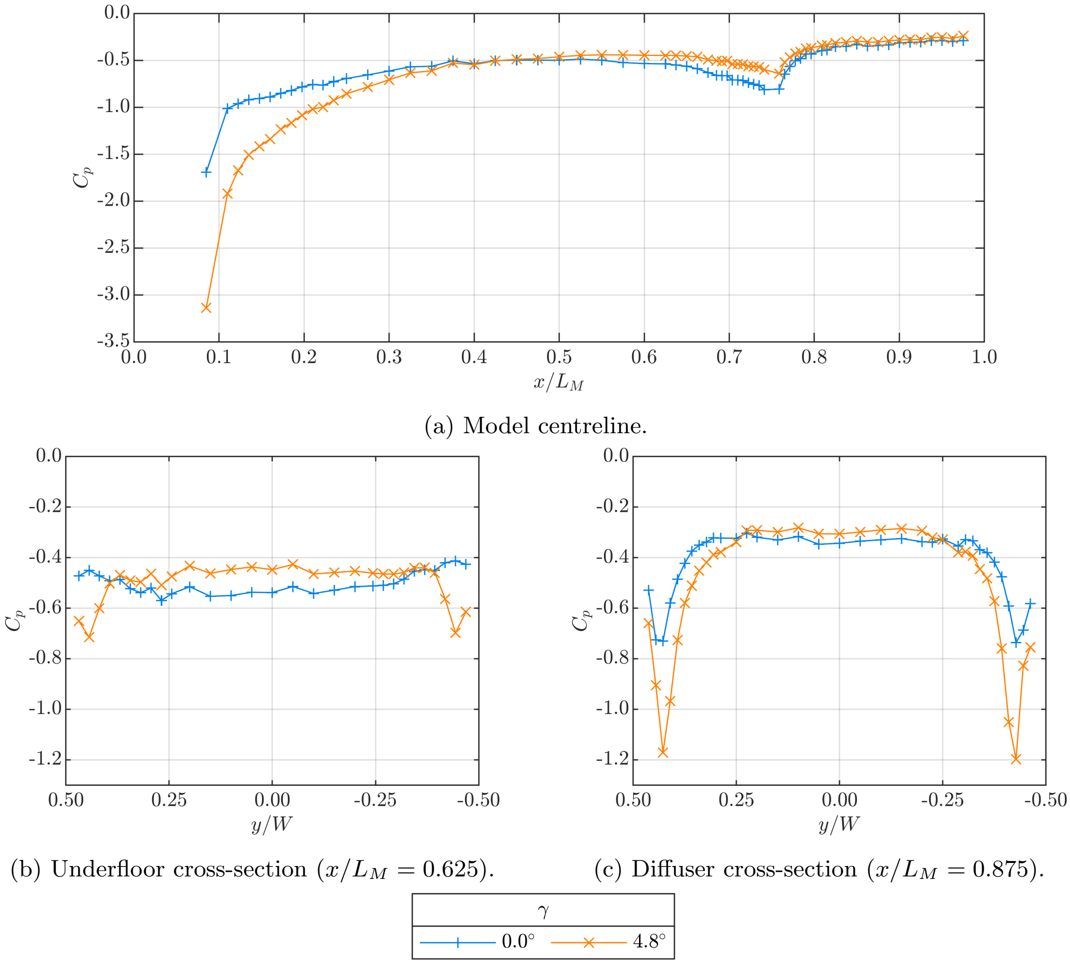

Figure 15: Plots of static pressure coefficient along the centreline and across the underfloor and the diffuser, at $h_1/H = 0.129$, $\theta = 16.3°$, and two rake angles.

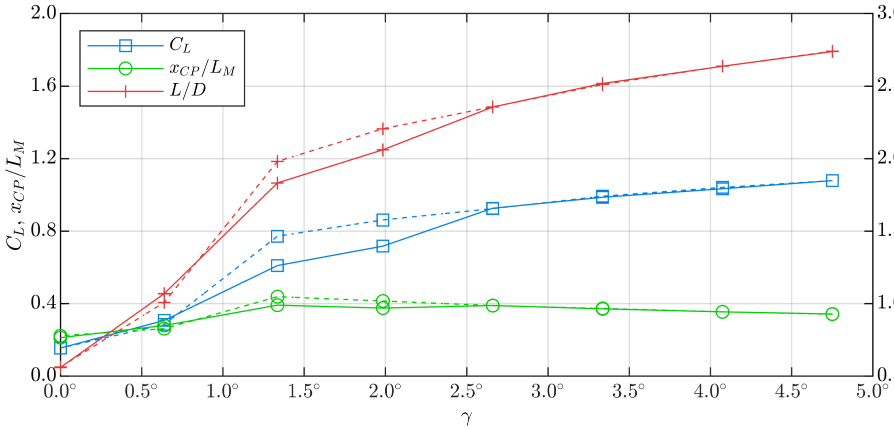

Figure 16: Plots of downforce coefficient, centre of pressure and aerodynamic efficiency against rake angle, at $h_1/H = 0.065$ and $\theta = 24.7°$.

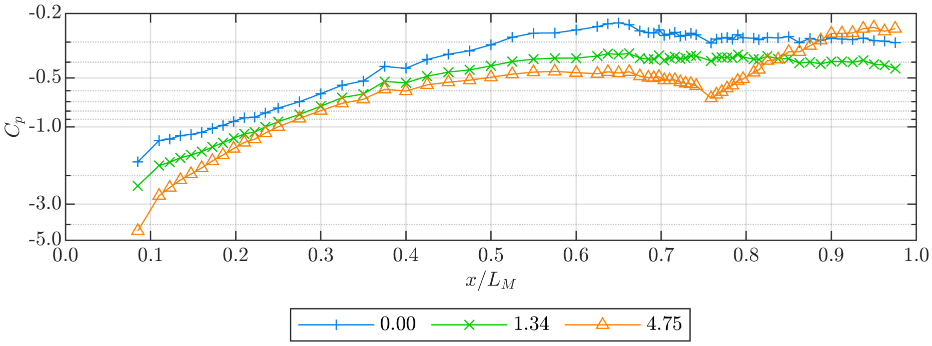

(a) Model centreline.

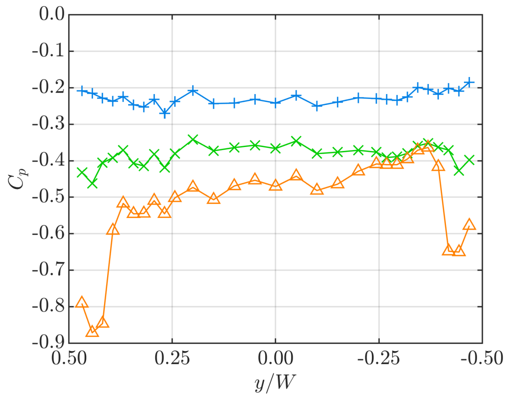

(b) Underfloor cross-section ($x/L_M = 0.625$).

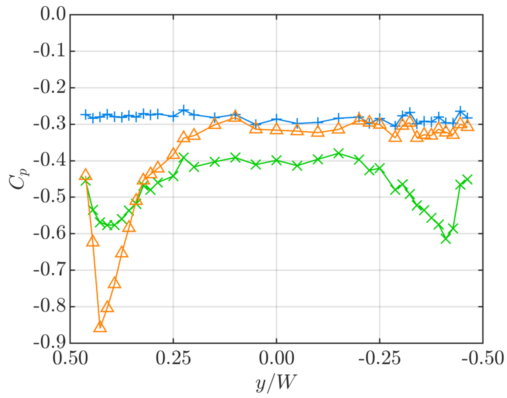

(c) Diffuser cross-section ($x/L_M = 0.875$).

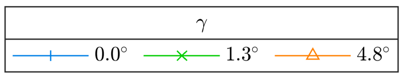

Figure 17: Plots of static pressure coefficient along the centreline and across the underfloor and the diffuser, at $h_1/H = 0.065$, $\theta = 24.7°$, and three rake angles.